

# Debris disc formation induced by planetary growth

H. Kobayashi<sup>1\*</sup> and T. Löhne<sup>2</sup>

<sup>1</sup> *Department of Physics, Nagoya University, Nagoya, Aichi 464-8602, Japan*

<sup>2</sup> *Astrophysical Institute and University Observatory, Friedrich Schiller University, Schillergaesschen 2-3, 07745 Jena, Germany*

Released 2002 Xxxxx XX

## ABSTRACT

Several hundred stars older than 10 million years have been observed to have infrared excesses. These observations are explained by dust grains formed by the collisional fragmentation of hidden planetesimals. Such dusty planetesimal discs are known as debris discs. In a dynamically cold planetesimal disc, collisional coagulation of planetesimals produces planetary embryos which then stir the surrounding leftover planetesimals. Thus, the collisional fragmentation of planetesimals that results from planet formation forms a debris disc. We aim to determine the properties of the underlying planetesimals in debris discs by numerically modelling the coagulation and fragmentation of planetesimal populations. The brightness and temporal evolution of debris discs depend on the radial distribution of planetesimal discs, the location of their inner and outer edges, their total mass, and the size of planetesimals in the disc. We find that a radially narrow planetesimal disc is most likely to result in a debris disc that can explain the trend of observed infrared excesses of debris discs around G-type stars, for which planet formation occurs only before 100 million years. Early debris disc formation is induced by planet formation, while the later evolution is explained by the collisional decay of leftover planetesimals around planets that have already formed. Planetesimal discs with underlying planetesimals of radii  $\sim 100$  km at  $\approx 30$  AU most readily explain the Spitzer Space Telescope 24 and  $70\ \mu\text{m}$  fluxes from debris discs around G-type stars.

**Key words:** Planet formation – Debris discs.

## 1 INTRODUCTION

The circumstellar discs observed around several hundred main sequence stars are mainly gas poor, faint discs, and are mostly revealed by excess infrared emission around the stars. Dust grains to which the observed emission is attributed have lifetimes much shorter than the ages of the central stars; dust grains are continuously replenished by collisional cascades from hidden planetesimals, approximately kilometer-sized or larger bodies. However, since gravity plays a dominant role in determining the outcome of planetesimal collisions, collisional fragmentation of planetesimals to start collisional cascades needs collisional velocities between planetesimals exceeding their surface escape velocities. Therefore, significant perturbations to increase the collisional velocities between planetesimals for collisional fragmentation are required for the formation of debris discs. Plausible candidates for the perturbations of planetesimals in debris discs are (i) an early stellar encounter (Kobayashi & Ida 2001), (ii) the existence of massive gaseous planets (e.g., Mustill & Wyatt 2009), and (iii) the formation of planetary

embryos in a planetesimal disc (e.g., Kenyon & Bromley 2004). In this paper, we focus on debris discs induced by planetary formation.

Planetesimals formed in a protoplanetary disc are expected to have low random motions. Collisions between planetesimals result in coagulation. Gravitational focusing and dynamical friction lead to runaway growth of planetesimals and the formation of a single planetary embryo in each annulus of the disc. Embryos continue growing by collisional accretion of leftover planetesimals, which themselves do not grow significantly. Once embryos become sufficiently massive, planetesimals start effective collisional fragmentation. Small bodies resulting from collisional fragmentation of planetesimals collide with each other and become smaller still. The collisional cascade grinds bodies down until radiation pressure from the host star blows them away.

The collisional cascade and the subsequent blow-out reduce the surface density of planetesimals in the disc. Along with this reduction, embryo growth stalls (e.g., Kobayashi et al. 2010) and the dust mass supplied by the collisional cascade decreases. On the other hand, the formation timescale of planetary embryos is longer in the outer disc; planetary growth propagates from the inner to

\* hkobayas@nagoya-u.jp

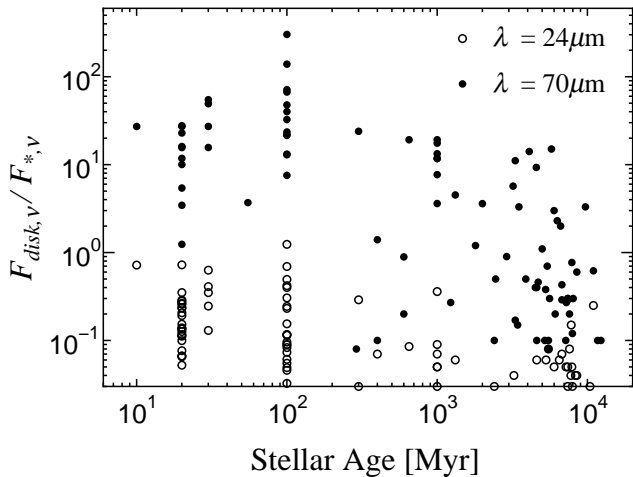


**Figure 1.** The ratios of disc fluxes  $F_{\text{disc},\nu}$  for G-type stars to the stellar fluxes  $F_{*,\nu}$  observed (but not necessarily detected) at both wavelengths  $\lambda = 24\ \mu\text{m}$  (open circles) and  $70\ \mu\text{m}$  (filled circles), as a function of the ages of host stars (Bryden et al. 2006; Chen et al. 2005a,b; Kim et al. 2005; Beichman et al. 2005, 2006; Meyer et al. 2004; Hines et al. 2006; Moro-Martín et al. 2007; Hillenbrand et al. 2008).

outer disc. When the dust mass produced by planet formation decreases in the inner disc, subsequent planet formation increases the dust production rate in the outer disc. Therefore, inside-out planet formation can maintain a detectable amount of debris in broad planetesimal discs (e.g., Kenyon & Bromley 2004, 2008). Note that the brightness evolution of debris discs depends on the broadness of initial planetesimal discs, as shown below.

Planetesimal formation is still a critical issue in the theory of planet formation. Recently, it has been shown that planetesimals may be formed from pebbles accumulated in vortices in a turbulent disc (e.g., Cuzzi, Hogan, & Shariff 2008) or by direct collisional coagulation of fluffy dust aggregates (Okuzumi et al. 2012). Planetesimal size depends on the formation process. In addition, planetesimal formation might occur in limited locations. The initial planetesimal size and spatial distribution influence the planetary embryo formation timescale and therefore the temporal evolution of a debris disc.

Infrared surveys by IRAS, ISO, the Spitzer Space Telescope and others have shown that infrared excesses from debris discs around main-sequence stars are common. In particular, various photometric surveys of hundreds of nearby stars have been conducted by the Spitzer Space Telescope. Although observations have been done for many types of stars, in this paper we are interested in planet formation around solar type stars, and thus we focus on debris discs around G-type stars. The observed infrared excesses mainly decay with stellar age (see Fig. 1). The time evolution of debris discs induced by planet formation depends on the radial profiles of the initial planetesimal discs, the initial sizes of planetesimals, and their total masses. Therefore, the temporal evolution of infrared excesses gives constraints on the conditions of planetesimal discs that produce planets and debris discs.

In this paper, we investigate the temporal evolution of debris discs induced by planet formation. In § 2, we esti-

mate the radii and masses of debris discs from observational Spitzer MIPS data. In § 3, we describe our collision model and the mass evolution of bodies through collisions. In § 4, we carry out simulations for debris disc formation induced by planetary embryo formation, and give constraints on initial conditions; the radii of the inner and outer edges of initial planetesimal disc, initial disc mass, and the initial radius of planetesimals. In § 5, we discuss the origin of the inner and outer edges of discs, such as gas depletion, early stellar encounters, and planetesimal formation, and their relation with the solar system.

## 2 DISC RADII AND MASSES

We consider an optically thin debris disc radially distributed from  $r_{\text{in}}$  to  $r_{\text{out}}$ . The received flux at frequency  $\nu$ ,  $F_{\text{disc},\nu}$ , from thermal emission of the disc around a central star at a distance  $D$  from the observer is given by

$$F_{\text{disc},\nu} = \frac{1}{D^2} \int_{r_{\text{in}}}^{r_{\text{out}}} \int_{s_{\text{min}}}^{s_{\text{max}}} 2\pi r C_g Q_{\text{abs},\nu} n_s(s,r) B_\nu(T) ds dr, \quad (1)$$

where  $C_g = \pi s^2$  is the geometrical cross section of a spherical grain with radius  $s$ ,  $Q_{\text{abs},\nu}$  is the absorption efficiency at frequency  $\nu$ ,  $n_s(s,r) ds$  is the surface number density of dust grains with sizes ranging from  $s$  to  $s + ds$  at a distance  $r$  from the central star,  $T$  is the dust temperature dependent on  $s$  and  $r$ ,  $B_\nu(T) = 2h\nu^3/c^2 (e^{h\nu/k_B T} - 1)^{-1}$  is the Planck function,  $c$  is the speed of light,  $h$  is the Planck constant, and  $k_B$  is the Boltzmann constant. The flux is sensitive to the smallest grain radius  $s_{\text{min}}$ , compared to the largest one  $s_{\text{max}}$ . In debris discs, dust grains are supplied from collisional fragmentation. Small grains with radius  $\lesssim 1\ \mu\text{m}$  are blown out by radiation pressure around the solar type star (e.g., Burns, Lamy, & Soter 1979; Kobayashi et al. 2008, 2009).

The temperature of dust particles is determined by the energy equilibrium between stellar radiation and thermal emission, given by

$$4 \int_0^\infty Q_{\text{abs},\nu} B_\nu(T) d\nu = \frac{R_*^2}{r^2} \int_0^\infty Q_{\text{abs},\nu} B_\nu(T_*) d\nu, \quad (2)$$

where the stellar radiation is assumed to be blackbody with effective temperature  $T_*$  and  $R_*$  is the radius of the central star. If the dust radius is much larger than the incident radiation wavelength  $\lambda = c/\nu$ ,  $Q_{\text{abs},\nu} \approx 1$ . For  $s \ll \lambda$ ,  $Q_{\text{abs},\nu} \approx 2\pi s k/\lambda$ , where  $k$  is the imaginary part of the complex refractive index (e.g., Bohren & Huffman 1983). For blackbody grain ( $Q_{\text{abs},\nu} = 1$ ), the temperature is independent of grain size and is given by  $T \approx 280(r/1\ \text{AU})^{-1/2} (R_*/R_\odot)^{1/2}$  K, where  $R_\odot$  is the solar radius.

The fluxes of debris discs around G-type stars,  $F_{\text{disc},\nu}$ , divided by host star fluxes  $F_{*,\nu}$  were obtained from published observations at 24 and  $70\ \mu\text{m}$  with the MIPS photometer of the Spitzer Space Telescope (see Fig. 1). The debris discs revealed by high-resolution imaging are narrow rather than broad and their dust size distributions are approximately given by a single power law due to collisional cascades. If we assume that  $r_{\text{in}} = r$ ,  $r_{\text{out}} = 1.1r$ ,  $s_{\text{min}} = 1\ \mu\text{m}$ ,  $s_{\text{max}} \gg s_{\text{min}}$ , and  $n_s(s,r) = A s^{-7/2}$  where  $A$  is a constant, we obtain  $r$  and  $A$  from flux ratios at 24 and  $70\ \mu\text{m}$ . Fig. 2 shows the radii ( $r$ ) and masses of observed disks. The disc masses correspond to the total masses of

grains smaller than 1 mm. Although  $Q_{\text{abs},\nu} = 1$  for blackbody grains, for realistic grains, we apply  $Q_{\text{abs},\nu}$  calculated from Mie theory using the complex refractive index of dirty ice<sup>1</sup> (Bohren & Huffman 1983). For bodies smaller than the peak wavelength of the thermal emission spectrum, grain temperatures calculated for dirty-ice grains are higher than those for blackbody grains. The disc radii obtained for dirty-ice grains are thus 2–5 times larger than those for blackbody grains. Disc masses estimated using dirty-ice grains are larger by an order of magnitude.

The dependence on stellar ages may indicate the evolution of discs. Disc radii decrease after several billion years and disc masses peak around 100 million years. However, it should be noted that we obtain disc radii and masses by excluding data with flux ratios smaller than 0.06 (0.15) for  $\lambda = 24 \mu\text{m}$  ( $70 \mu\text{m}$ ) due to observational uncertainty (Bryden et al. 2006). Discs around older stars mainly have flux ratios lower than the limit for  $\lambda = 24 \mu\text{m}$  because of large disc radii. Therefore, we cannot obtain radii and masses of most old discs through this analysis.

### 3 MODEL

In debris discs, small grains are removed within a short timescale mainly by collisional fragmentation and radiation pressure. Kilometer-sized or larger parent bodies are required to maintain debris discs in timescales comparable to the ages of their host stars. Parent bodies with low random motions initially undergo collisional growth, rather than fragmentation, and then planets are formed via runaway/oligarchic growth. Once planets are substantially massive, leftover planetesimals start collisional fragmentation, resulting in debris disc formation. In this section, we describe our model of the outcomes of single collisions and the mass evolution of bodies through collisions to investigate thermal flux evolution caused by planet formation in planetesimal discs.

#### 3.1 Mass Evolution of Bodies and Collisional Outcomes

The formation and growth of planetary embryos that induce dust production in a planetesimal disc are investigated via statistical simulation developed in Kobayashi et al. (2010). The mass evolution of bodies is caused by mutual collisions dependent on the random velocities of bodies, which are affected by the mass distribution of bodies. The mass and velocity evolution is therefore coupled. Although we do not follow the orbits of bodies, our simulation that calculates the mass and velocity evolution can reproduce the embryo formation results of  $N$ -body simulation (Kobayashi et al. 2010).

The random velocities of planetesimals, determined by

orbital eccentricities and inclinations, increase due to stirring by planetary embryos, which induce collisional fragmentation. Collisions between already fragmented bodies made them even smaller. Once fragments are smaller than  $\sim 1 \mu\text{m}$  in radius, they are no longer bound to the host star due to the contribution of radiation pressure and are mainly blown out before being destroyed in mutual collisions (e.g., Burns, Lamy, & Soter 1979). Therefore, such a collisional cascade reduces the total mass of planetesimals. Although the mass reduction in some previous studies had been investigated under the assumption that catastrophic collisions are dominant, Kobayashi & Tanaka (2010) found that weak erosive collisions are more important for the mass reduction of planetesimals by collisional cascades. They obtained an analytical solution for the mass reduction including erosive collisions, and this is reproduced by our simulations. Therefore, we can accurately follow both planet formation and debris production.

Dust production is mainly determined by the total ejecta mass,  $m_e$ , from a single collision between bodies with masses  $m_1$  and  $m_2$ , given by

$$m_e = \frac{\phi}{1 + \phi}(m_1 + m_2). \quad (3)$$

Here  $\phi = m_1 m_2 v_{\text{col}}^2 / 2(m_1 + m_2)^2 Q_{\text{D}}^*$  is the scaled impact energy, where  $Q_{\text{D}}^*$  is the specific impact energy required for the ejection of half of the mass of the colliders and  $v_{\text{col}}$  is the impact velocity. Collisional simulations of dust aggregates (very small particles) suggest that  $Q_{\text{D}}^*$  is independent of aggregate size and of order  $10^7 \text{erg/g}$  (Wada et al. 2013). For large bodies,  $Q_{\text{D}}^*$  is purely determined by gravity and is thus proportional to the square of the surface escape velocity. For intermediate-sized bodies (1 cm–100 km in radius), hydrodynamic simulations show that  $Q_{\text{D}}^*$  increases with radius,  $s$ , for  $s > 0.1$ –1 km, while  $Q_{\text{D}}^*$  decreases with  $s$  for  $s < 0.1$  km. Therefore, we model

$$Q_{\text{D}}^* = Q_s \left[ 1 + \left( \frac{s}{1 \text{ cm}} \right)^{-b_s} \right]^{-1} + \rho \left[ Q_{\text{g},1} \left( \frac{s}{1 \text{ cm}} \right)^{b_{\text{g},1}} + Q_{\text{g},2} \left( \frac{s}{1 \text{ cm}} \right)^2 \right], \quad (4)$$

where  $\rho$  is material density and  $Q_s$ ,  $b_s$ ,  $Q_{\text{g},1}$ ,  $b_{\text{g},1}$ , and  $Q_{\text{g},2}$  are constants. We apply  $Q_s = 1.6 \times 10^7 \text{erg/g}$ ,  $b_s = -0.39$ ,  $Q_{\text{g},1} = 1.2 \text{erg cm}^3/\text{g}^2$ , and  $b_{\text{g},1} = 1.26$  based on Benz & Asphaug (1999), and  $Q_{\text{g},2} = 5.0 \times 10^{-3} \text{erg cm}^3/\text{g}^2$  based on Stewart & Leinhardt (2009).

We investigate the collisional evolution of bodies in a disc after gas depletion. Since the eccentricities of planetesimals increase to as much as unity, we take into account the reduction of the surface density of planetesimals due to scattering from planetary systems. According to the results of  $N$ -body simulations by Ida & Makino (1992), the eccentricities of bodies in each mass bin have a Rayleigh distribution. The fraction of bodies with eccentricities larger than unity is negligible for a small mean value of the distribution, while the fraction is significant for a mean value close to unity. If the mean eccentricity becomes larger than 0.25, we remove the fraction of bodies with eccentricities larger than unity and set a new mean eccentricity determined by the leftover bodies.

<sup>1</sup> The composition of dirty ice is ice, organics, and silicates, whose volume ratio is set to be 2:1:1 according to the local interstellar cloud (Kimura, Mann, & Jessberger 2003). The complex refractive index of dirty ice is calculated using those of ice (Warren 1984), organic refractory material (Li & Greenberg 1997), and astronomical silicate (Draine & Lee 1984) through the Maxwell-Garnett mixing rule.

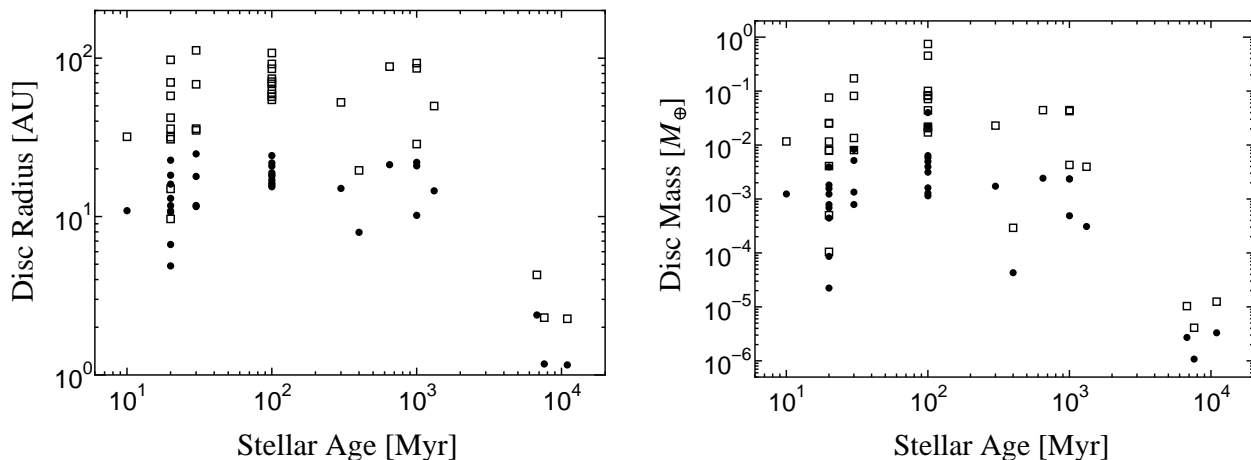


**Figure 2.** Disc radii and masses obtained from observational data with flux ratio larger than 0.06 (0.15) for  $\lambda = 24 \mu\text{m}$  ( $70 \mu\text{m}$ ) in Fig. 1 for dirty-ice grains (open squares) and blackbody grains (filled circles), as a function of host star age.

### 3.2 Optical Depth and Thermal Emission

In our simulations, we follow the evolution of the optical depth  $\tau$ , where

$$\tau(r) = \int_{s_{\min}}^{s_{\max}} C_g n_s(s, r) ds. \quad (5)$$

Substituting  $\tau$  into Eq. (1), the disc flux is re-written as

$$F_{\text{disc}, \nu} = \frac{1}{D^2} \int_{r_{\text{in}}}^{r_{\text{out}}} 2\pi r \tau(r) S_\nu(r) dr, \quad (6)$$

where

$$S_\nu(r) = \left[ \int_{s_{\min}}^{s_{\max}} C_g Q_{\text{abs}, \nu} n_s(s, r) B_\nu(T) ds \right] \times \left[ \int_{s_{\min}}^{s_{\max}} C_g n_s(s, r) ds \right]^{-1}. \quad (7)$$

For blackbody dust,  $S_\nu(r) = B_\nu(T)$  for  $T$  corresponding to the temperature at  $r$ . Even for realistic dust, if the size distribution of  $n_s(s, r)$  is known,  $S_\nu(r)$  can be obtained. We use  $S_\nu(r)$  obtained from the temperature of dirty ice dust and the assumption that  $n_s \propto s^{-7/2}$ . Although our simulations yield size distributions, we use the simple  $S_\nu(r)$  to save computational cost in fitting over a wide parameter range in §4.2. Since there is no significant difference between the simple and realistic  $S_\nu$ , our treatment does not affect the results. Note that we directly obtain  $\tau$  from simulations because the error of  $\tau$  estimated from large bodies under the power-law assumption is much greater than that of the simple  $S_\nu$ .

Active radial transport of bodies occurs via interaction with gas in protoplanetary discs or by the Poynting-Robertson effect in gas-free discs. Hence, simulations with multiple annuli are required. However, the radial drift of bodies is negligible in most observed discs because the collisional timescale is shorter than the radial drift timescale due to the Poynting-Robertson effect for  $\tau \gtrsim 3 \times 10^{-5} (r/10 \text{ AU})^{-1/2}$  (Wyatt 2005). We thus ignore radial transport in our simulations.

## 4 RESULT

### 4.1 Evolution of Optical Depth

We simulate the formation of planets and a debris disc at  $r = 10 \text{ AU}$  in a disc with  $\Sigma = 0.95 \text{ g cm}^{-2}$ , equivalent to the solid surface density in the minimum-mass solar nebula model (Hayashi 1981). Since the size distribution of bodies is narrow prior to runaway growth of planetesimals, we set a single size population of planetesimals with radius  $s_0 = 10 \text{ km}$  at the beginning of the simulation. In the simulation, the radius of the smallest bodies is set to be  $1 \mu\text{m}$ , below which dust grains are blown out on a Keplerian timescale.

The cumulative surface density and optical depth of bodies larger than a given radius  $s$  with eccentricities  $e$  and inclinations  $i$  are shown in Fig. 3. Planetary embryos of radii  $\sim 10^3 \text{ km}$  form in  $\sim 10^7$  years but then the surface density is mainly determined by bodies of  $\sim 10 \text{ km}$ : Runaway growth produces massive embryos but most remaining bodies retain the initial size almost without growth. The stirring of massive embryos increases  $e$  and  $i$  of leftover planetesimals and induces their collisional fragmentation. The collisional cascade of bodies smaller than  $10 \text{ km}$  reduces the surface density and optical depth of the disc within a timescale of several  $10^7$  years.

Figure 4 shows the evolution of planetary embryo mass<sup>2</sup> and optical depth  $\tau$  at 5, 10, and 20 AU. Planetary embryos initially grow exponentially (runaway growth) but subsequently they grow slowly due to the high  $e$  and  $i$  of stirred planetesimals (oligarchic growth). Once embryo masses reach  $\sim 10^{-3} M_\oplus$ , the optical depth rapidly increases due to collisional fragmentation of planetesimals induced by embryo formation. Finally, their growth is stalled due to the reduction of the surface density of planetesimals caused by collisional cascade, which gradually reduces the optical depth.

Debris disc formation induced by planet formation was also investigated in previous studies (Kenyon & Bromley

<sup>2</sup> We define planetary embryo mass as the average mass of “runaway bodies” that can have orbital separations of 10 Hill radii (see Kobayashi et al. 2010).

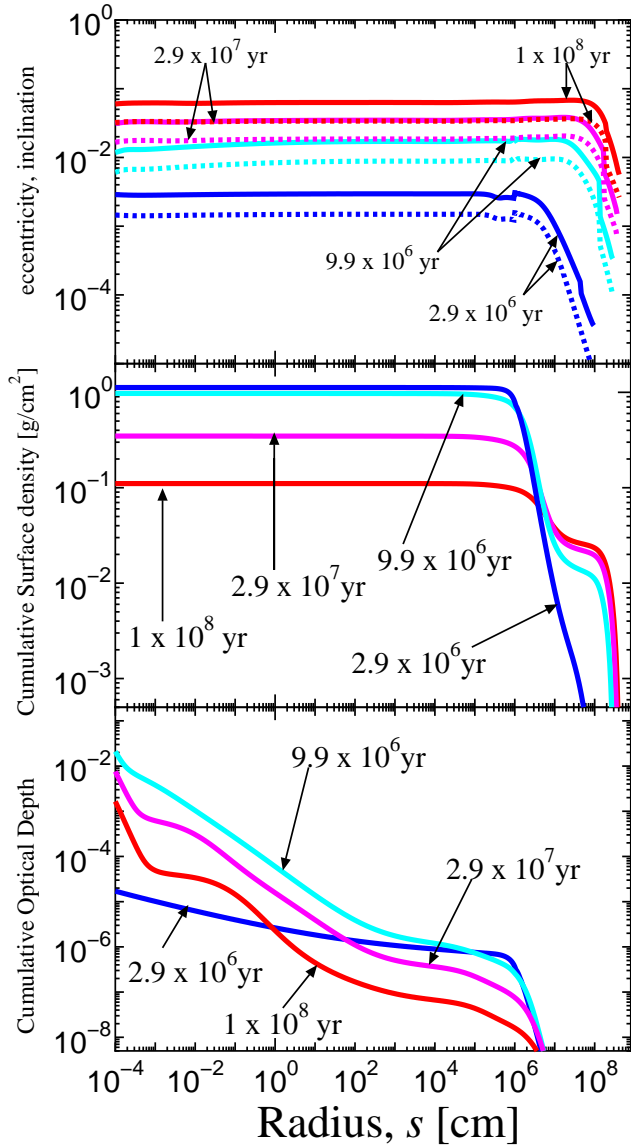


**Figure 3.** Eccentricity (solid curves, top panel), inclinations (dotted curves, top panel), and the cumulative surface density (middle panel) and optical depth (bottom panel) of bodies larger than a given radius  $s$  at  $r = 10$  AU in a disc of planetesimals with initial radius 10 km and the initial surface density  $\Sigma = 0.95 \text{ g cm}^{-2}$ .

2004, 2008; Weidenschilling 2010). Due to high computational costs, the radii of the smallest bodies in their simulations were set to be much larger than the blow-out size. The authors mainly determined the evolution of the resultant smaller bodies based on the theory of collisional cascades (power law distribution). However, the distribution does not follow the power law distribution before the onset of active collisional fragmentation due to planet formation and even for collisional equilibrium the distribution has wavy structures around the blow-out size (Löhne, Krivov, & Rodmann 2008). To calculate optical depth accurately, bodies larger than the blow-out size should be followed in a simulation. Therefore, we treat all bodies larger than the blow-out size (1  $\mu\text{m}$  in radius).

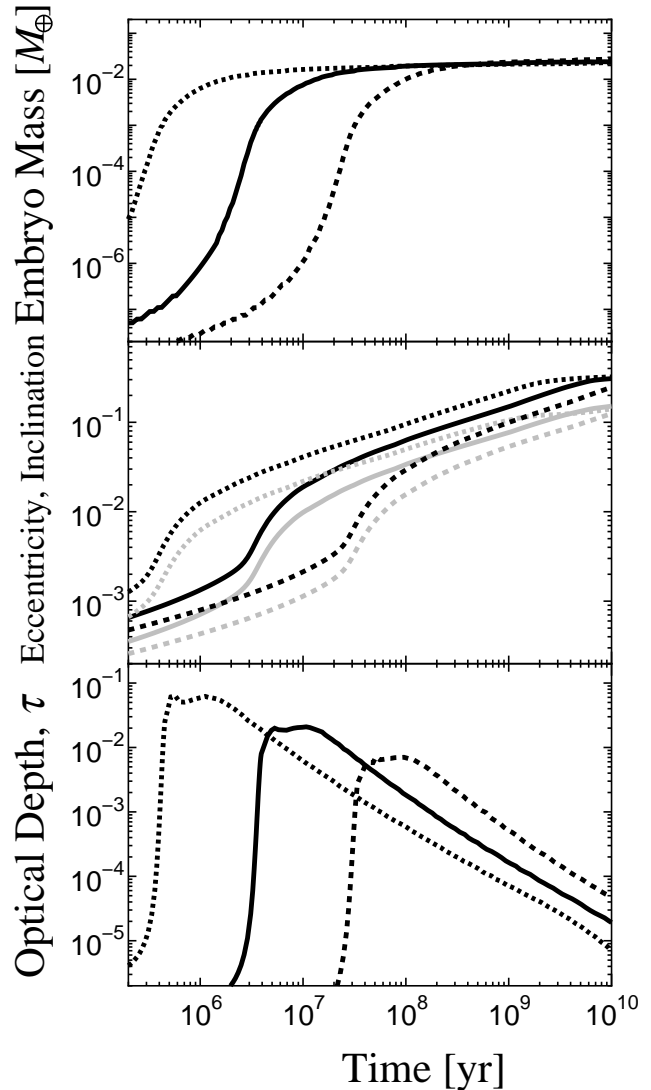


**Figure 4.** Evolution of planetary embryo mass (top panel), eccentricity (black) and inclination (gray) of 10 km-radius bodies (middle panel), and optical depth  $\tau$  (bottom panel), starting from 10 km-radius planetesimals for  $\Sigma = 2.7 \text{ g cm}^{-2}$ ,  $r = 5$  AU (dotted curves),  $\Sigma = 0.95 \text{ g cm}^{-2}$ ,  $r = 10$  AU (solid curves), and  $\Sigma = 0.34 \text{ g cm}^{-2}$ ,  $r = 20$  AU (dashed curves), where  $\Sigma$  is the solid surface density.

The rapid increase in  $\tau$  is caused by embryo formation via runaway growth. We empirically know that the growth timescale is inversely proportional to  $\Sigma\Omega$  in runaway growth (e.g., Ormel, Dullemond, & Spaans 2010), where  $\Omega$  is the Keplerian frequency. On the other hand,  $\tau$  gradually decreases on a collisional timescale, that is inversely proportional to  $\Sigma\Omega$  (Kobayashi & Tanaka 2010). The optical depth is expected to be proportional to  $\Sigma$ . Therefore, we scale the temporal evolution of  $\tau$ . As shown in Fig. 5, the scaled temporal evolution is in good agreement with the actual simulation. Owing to this scaling, numerous simulations with different annular radii and surface densities are not necessary to treat a broad disc: We can calculate evolutionary fluxes for each choice of disc parameter based on the time evolution of  $\tau$  given by a single simulation.

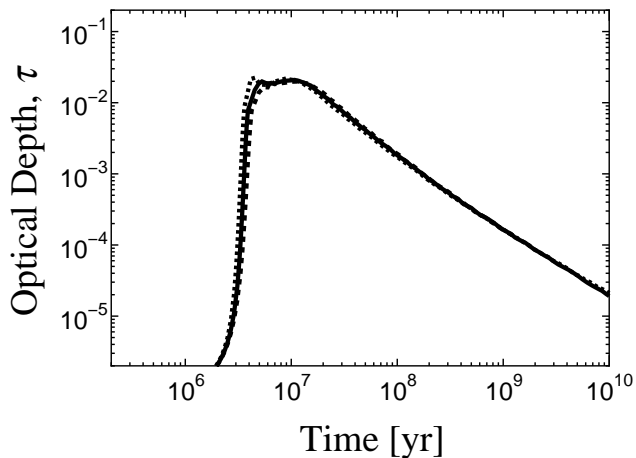


**Figure 5.** Same as the bottom panel of Fig. 4, but optical depth  $\tau$  and time  $t$  are divided by  $(\Sigma/0.95 \text{ g cm}^{-2})$  and  $(\Sigma/0.95 \text{ g cm}^{-2})^{-1}(r/10 \text{ AU})^{3/2}$ , respectively.

It should be noted that the temporal evolution of  $\tau$  depends on the initial planetesimal radius  $s_0$ , as shown in Fig. 6. For smaller  $s_0$ , runaway growth occurs earlier and thus  $\tau$  increases earlier. Once active dust production occurs, more frequent collisions of more fragile planetesimals (lower  $Q_D^*$ ) for smaller  $s_0$  lead to higher dust production: Smaller  $s_0$  results in higher  $\tau$ , whereas  $\tau$  decays earlier for smaller  $s_0$ . For  $s_0 \lesssim 10 \text{ km}$ ,  $\tau$  increases along with runaway growth of planetesimals, while  $\tau$  increases prior to runaway growth for larger planetesimals. When the runaway growth starts, planetesimals have random velocities  $v_r = \sqrt{e^2 + i^2} v_k$  as large as the surface escape velocity,  $v_{\text{esc}}$ , of the planetesimals, where  $v_k$  is the Keplerian velocity. Since their specific impact energies at the beginning of runaway growth are much smaller than  $Q_D^*$  of planetesimals with  $s_0 \lesssim 10 \text{ km}$ ,  $\tau$  is very low before runaway growth and suddenly increases at the onset of runaway growth. For  $s_0 \gtrsim 100 \text{ km}$ , the specific impact energy is slightly smaller than or comparable to  $Q_D^*$  of initial planetesimals at the beginning of runaway growth. Due to collisional erosion of planetesimals, collisional cascades increase  $\tau$  prior to runaway growth, resulting in the small peak value of  $\tau$ . Therefore, the dependence of  $\tau$  evolution on  $s_0$  is complicated, because fragmentation efficiency of planetesimals determined by  $Q_D^*$  depends on  $s_0$ . Although we cannot derive a formula for  $s_0$  dependence, the scaling for  $\Sigma$  and  $r$  is valid for each value of  $s_0$ .

#### 4.2 Evolution of Disc Flux

We obtain the disc flux by the integration of  $\tau$  over  $r$  using Eq. (6). For the integral, we introduce a power-law surface density model of

$$\Sigma = x \Sigma_{10} \left( \frac{r}{10 \text{ AU}} \right)^{-p}, \quad (8)$$

where  $\Sigma_{10} = 0.95 \text{ g cm}^{-2}$  is the reference surface density at 10 AU, corresponding to that at 10 AU in the minimum mass solar nebula model (Hayashi 1981), and  $x$  is a scaling parameter.

Figure 7 shows the temporal evolution of flux from a wide disc from 5 to 100 AU and from a narrow disc from 10 to

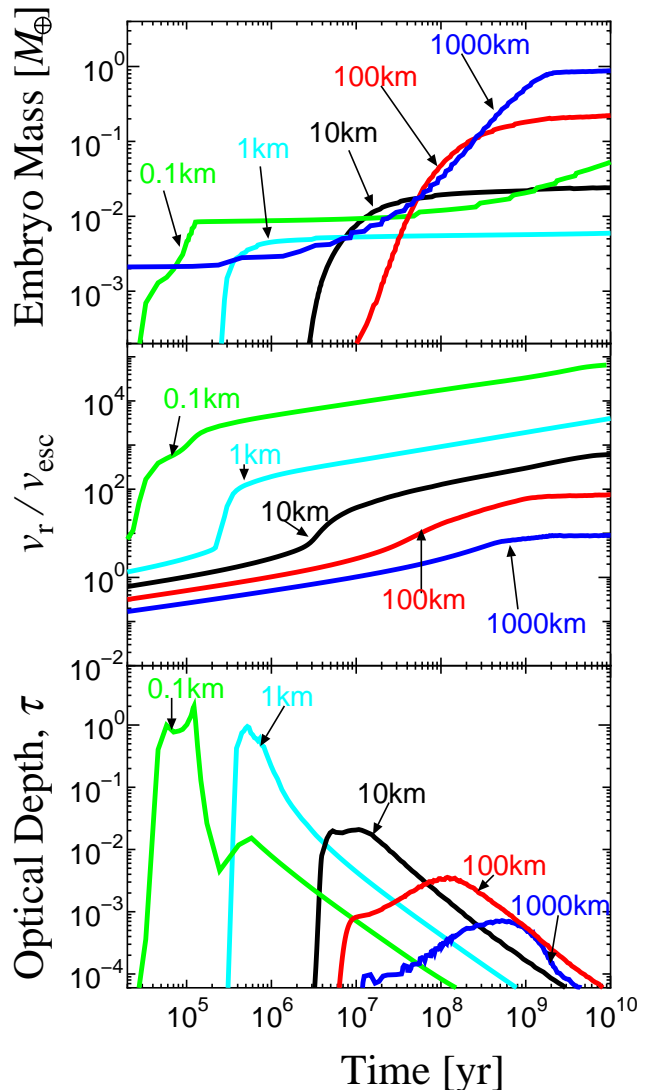


**Figure 6.** Temporal evolution of embryo mass (top), the ratio of random velocity  $v_r$  of bodies with initial radii  $s_0$  to their surface escape velocity  $v_{\text{esc}}$  (middle), and optical depth (bottom) for different initial planetesimal radii  $s_0 = 0.1$ –1000 km with  $\Sigma = 0.95 \text{ g cm}^{-2}$  at 10 AU.

50 AU with  $x = 1$  and  $p = 1.5$ , initially composed of 10 km-radius planetesimals ( $s_0 = 10 \text{ km}$ ). The fluxes increase at around  $10^6$  years for the wide disc, but 10 times later for the narrow disc. This is caused by planet formation around the inner edges of the discs. The vertical optical depth around the inner edges gradually decreases after planet formation occurs (see Fig. 4), while planet formation propagates to the outer disc. This growth propagation maintains high fluxes until the growth front reaches the outer, cold disc or the outer edge of the disc. For the  $24 \mu\text{m}$  flux, thermal emission from the disc beyond several 10 AU has a smaller contribution. Since the growth front reaches the cold region, the flux decreases after 100 million years. On the other hand,  $70 \mu\text{m}$  thermal emission from cold disc has a larger contribution. The flux decreases when planetary formation has finished at the outer edge of disc.

Fig. 8 shows the flux ratio evolution for different radial

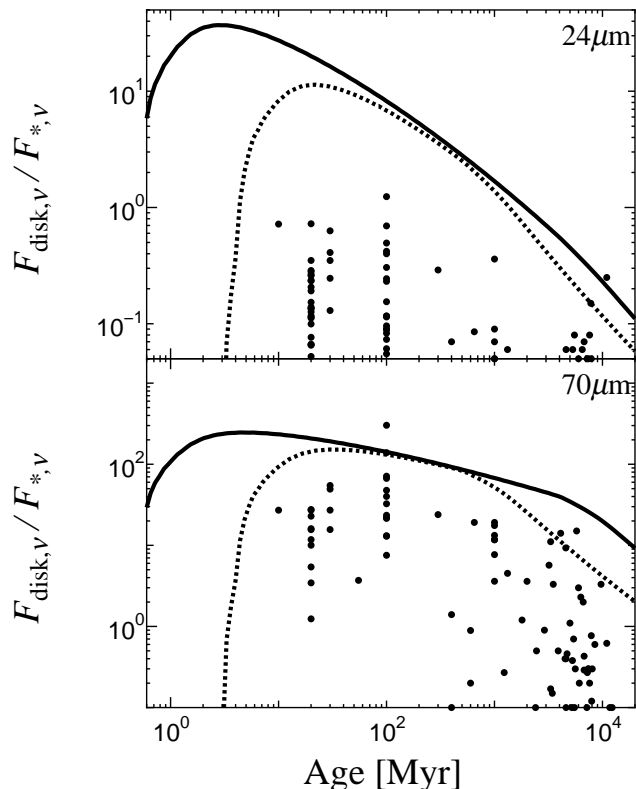


**Figure 7.** Temporal evolution of flux ratios at 24  $\mu\text{m}$  (top) and 70  $\mu\text{m}$  (bottom) for  $s_0 = 10$  km,  $x = 1$ , and  $p = 1.5$  in a wide disc ( $r_{\text{in}} = 5$  AU and  $r_{\text{out}} = 100$  AU; solid curves) and a narrow disc ( $r_{\text{in}} = 10$  AU and  $r_{\text{out}} = 50$  AU; dotted curves). Circles indicate the observational data shown in Fig. 1.

distributions of surface density. Since the surface densities at the inner edge are different, the flux ratios rise later for large  $p$ . After the rapid rise of flux ratios, growth propagation in the disc determines the flux ratio evolution. For 70  $\mu\text{m}$ , the flux ratios decrease for  $p \geq 1$ , while the ratio increases for  $p = 0$ .

Since the flux ratios from discs with  $x = 1$  are much larger than those obtained from observations, we further investigate the temporal evolution of flux ratios for less massive discs (Fig. 9). The maximum flux ratios decrease with decreasing  $x$ , while flux ratios rise later for smaller  $x$  because of a longer planet growth timescale. In order to explain lower observational flux ratios at 10–100 million years, small  $x$  and  $r_{\text{in}}$  are necessary: The flux evolution for  $x = 10^{-3}$  and  $r_{\text{in}} = 1$  AU seems more reasonable. However, the model fluxes are relatively high at 24  $\mu\text{m}$  and too low at 70  $\mu\text{m}$ , compared to observational data: The model disc radius is smaller than those estimated from the observational data. Indeed, while the disc radii estimated from observational data are much larger than 5 AU at 10–100 million years (see Fig. 2), the model flux with  $x = 10^{-3}$  comes from the disc inside 5 AU before 1 billion years.

The temporal flux evolution depends on the initial size of planetesimals (Fig. 10). For small planetesimals, planetary formation starts at the inner edge early and, of course, the growth front reaches the outer edge early. For  $s_0 = 0.1$  and 1 km, the fluxes are very high before 10 million years and

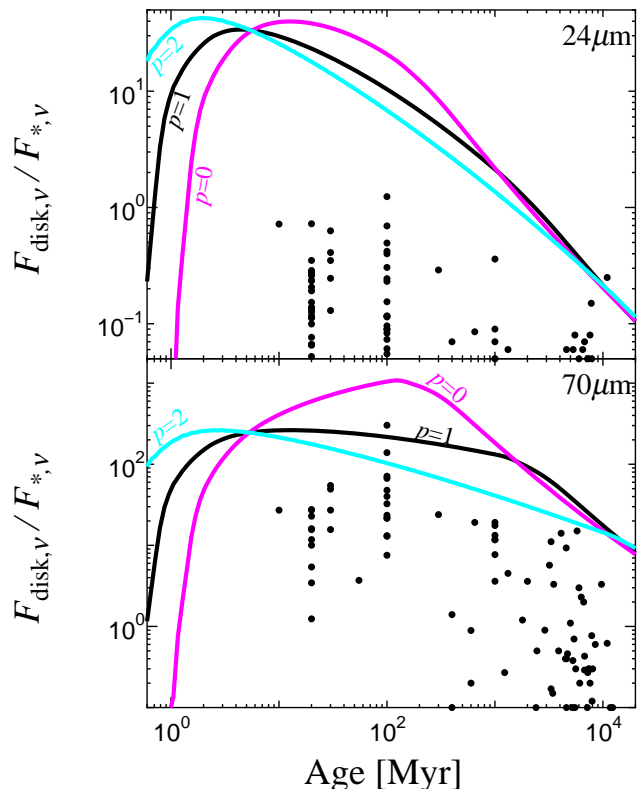


**Figure 8.** Dependence of flux evolution on  $p$  for  $s_0 = 10$  km,  $x = 1$ ,  $r_{\text{in}} = 5$  AU and  $r_{\text{out}} = 100$  AU.

then start decreasing at  $10^8$ – $10^9$  years: These model fluxes are much larger than observational ones before  $10^9$  years. On the other hand, the fluxes increase later for larger planetesimals and the fluxes remain high even after  $10^9$  years: The model fluxes significantly exceeds observational ones after  $10^8$  years. Therefore, the smooth discs seem unlikely to explain the observational data even for a wide range of initial planetesimal sizes (0.1–1000 km).

### 4.3 A Typical Disc

For each initial planetesimal radius, the most likely parameters to explain the observational data are found using a Monte-Carlo method for  $x = 10^{-4}$ –100, disc edge radii  $r_{\text{in}}$  and  $r_{\text{out}}$  ranging from 5 AU to 400 AU, and  $p = 0$ –2. From  $\chi^2$  tests, we obtain the best-fit parameters for the averaged data of the flux ratios at 24 and 70  $\mu\text{m}$  and their ratios in age bins<sup>3</sup>. Note that our best fit disc is no attempt to cover the observed variety of disc radii and masses with a single set of disc parameters. Instead it is meant to represent a typical or average disc.

<sup>3</sup> The mean values are  $(\log_{10} \text{Age}[\text{yr}], \log_{10} F_{\text{disc},\nu}/F_{*,\nu}|_{24\mu\text{m}}, \log_{10} F_{\text{disc},\nu}/F_{*,\nu}|_{70\mu\text{m}}) = (7.32, -0.63, 1.17), (8.03, -0.73, 1.55), (9.02, -1.27, 0.70)$ , and  $(9.80, -1.39, -0.51)$ , which are obtained from the average of logarithmic values for age bins,  $\log_{10} \text{Age}[\text{yr}] = 6.5$ –7.5, 7.5–8.5, 8.5–9.5, and 9.5–10.5. For averaging, we use all data if the flux ratios exceed 0.15 at 70  $\mu\text{m}$ , and we adopt 0.03 for the flux ratios at 24  $\mu\text{m}$  if they are smaller than 0.06.

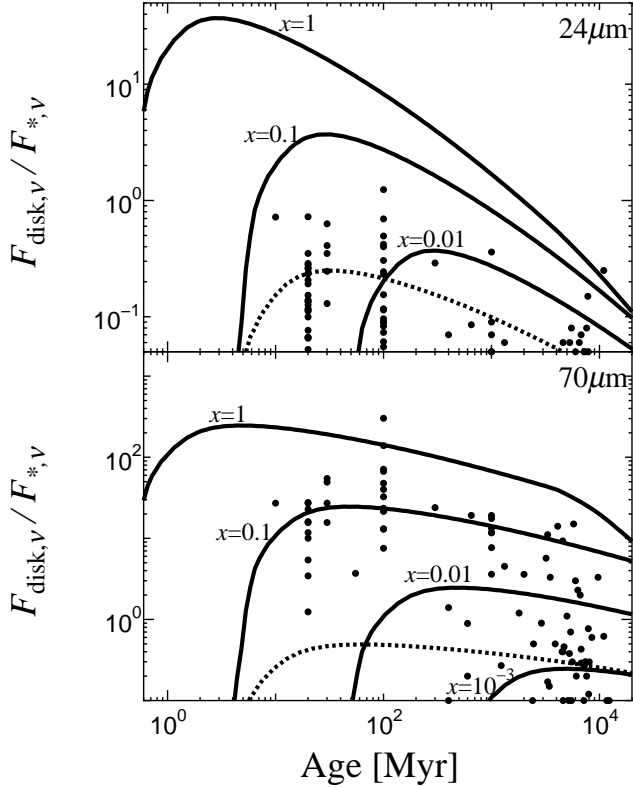


**Figure 9.** Dependence of flux evolution on  $x$  ranging from  $10^{-3}$  to 1 for  $s_0 = 10$  km,  $p = 1.5$ ,  $r_{\text{in}} = 5$  AU, and  $r_{\text{out}} = 100$  AU (solid curves). For  $x = 10^{-3}$ , the flux ratio at  $\lambda = 24$   $\mu\text{m}$  is below 0.05. Since the planet formation timescale becomes longer for low  $x$ , we also apply a smaller inner disc radius of  $r_{\text{in}} = 1$  AU for  $x = 1 \times 10^{-3}$  (dotted curve).

The likely parameter sets for several values of the initial planetesimal radius  $s_0$  are listed in Table 1. Fig. 11 shows the flux-ratio evolution for these likely parameters. Narrow discs are most likely to reproduce the observed fluxes. Due to the narrowness, the  $\chi^2$  values are similar for broad ranges of  $p$  and  $x$  as long as the total planetesimal mass  $M_{\text{tot}}$  is the same: The best fits are achieved for the relation  $M_{\text{tot}} = 2\pi x \Sigma_{10} (10 \text{ AU})^p (r_{\text{out}}^{2-p} - r_{\text{in}}^{2-p}) / (2-p)$ . The errors for  $p$  and  $x$  are not described in Table 1 because of correlation. They can be evaluated using the above relation. The smallest  $\chi^2$  values are obtained for  $s_0 = 0.1$  km, which is achieved in a very narrow parameter space. This is caused by the absence of fitted data at around 30–90 million years. If we exclude this parameter space, cases with  $s_0 = 100$  km best represent observations. For  $s_0 = 100$  km the  $\chi^2$  values near minimum are achieved for the wide range of  $M_{\text{tot}}$  (see Table 1). Therefore, the most likely initial planetesimal size seems to be of order 100 km.

## 5 DISCUSSION

Planetary embryos formed via runaway growth in a planetesimal disc induce collisional fragmentation of planetesimals that can supply dust grains to a debris disc. Planet formation propagates from the inner to outer disc, and the dust supply region moves in turn with planet formation.

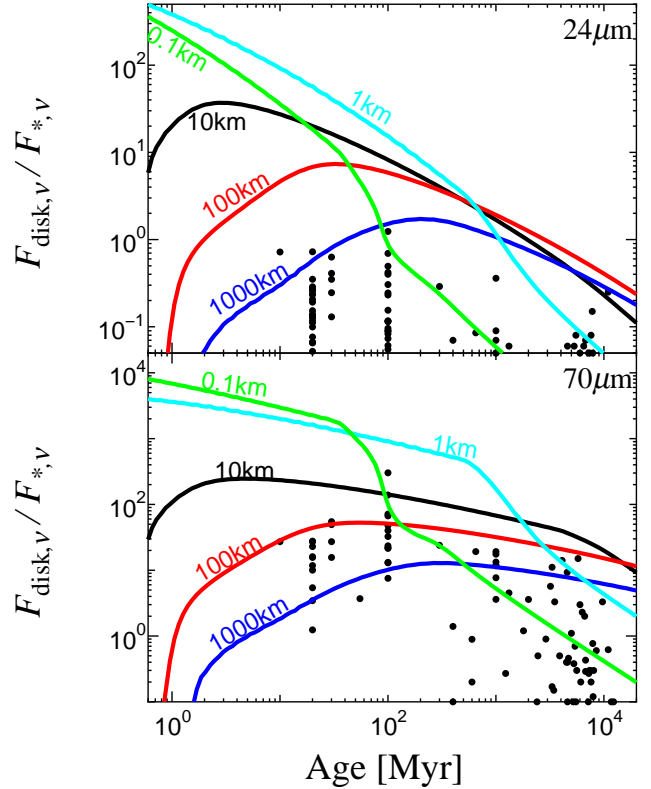


**Figure 10.** Dependence of flux evolution on  $s_0$  ranging from 0.1 to 1000 km for  $x = 1$ ,  $p = 1.5$ ,  $r_{\text{in}} = 5$  AU, and  $r_{\text{out}} = 100$  AU.

Since collisional fragmentation reduces the surface density of planetesimals, the dust production rate gradually decreases after planet formation occurs. As a result, planet formation forms narrow debris discs from inside out if initial planetesimal discs have a smooth radial distribution or have no radial cutoff. However, we find that planetesimal discs are likely narrow to account for most observational fluxes of debris discs around G-type stars. Planet formation in narrow planetesimal belts can also better explain debris discs around A-type stars (Kennedy & Wyatt 2010). For G stars, the plausible disc radii are estimated in this paper to be 25–35 AU for an initial planetesimal radius of  $s_0 \gtrsim 10$  km, whereas they are 40–80 AU for smaller initial planetesimals. Their radii are comparable to those obtained from the simple estimate shown in § 2, whereas the total mass of bodies is not well determined from the simple estimate because of the uncertainty of the size distribution of large bodies (see Fig. 2 and Table 1). In addition, from more detailed analyses we find that 100 km sized planetesimals are most likely to explain the observational fluxes.

The fluxes of debris discs are mainly determined by thermal emission of dust grains of size 1–100  $\mu\text{m}$ . However, in previous studies, the debris disc fluxes caused by planet formation are calculated by extrapolation from the results of simulations that only treat bodies larger than  $\sim 1$  m (Kenyon & Bromley 2004, 2008). Therefore, their model fluxes are underestimated by a factor 3–10, compared to simulations handling down to 1  $\mu\text{m}$ -sized dust grains. On the other hand, previous simulations included a gaseous component with a lifetime of  $10^7$  years, while we ignore the



**Table 1.** The best-fit parameters to observational data: For each initial planetesimal radius  $s_0$ , the inner and outer radii of the disc  $r_{\text{in}}$  and  $r_{\text{out}}$ , the surface density scaling factor  $x$ , the surface density radial slope  $-p$ , and the total mass  $M_{\text{tot}}$  of the initial planetesimal disc are listed. The errors for  $x$  and  $p$  are discussed in the main text.

$s_0$ [km]	$r_{\text{in}}$ [AU]	$r_{\text{out}} - r_{\text{in}}$ [AU]	$x$	$p$	$M_{\text{tot}}$ [ $M_{\oplus}$ ]
0.1	$70.6^{+1.3}_{-0.04}$	$13.5^{+0.03}_{-5.1}$	0.23	1.1	$5.7^{+0.5}_{-0.2}$
1	$39.6^{+0.7}_{-0.8}$	$1.47^{+1.33}_{-0.77}$	0.40	0.56	$14^{+0.01}_{-1.5}$
10	$34.3^{+0.1}_{-0.8}$	$2.23^{+1.53}_{-0.12}$	1.34	0.04	$33^{+2.9}_{-1.8}$
100	$30.5^{+0.7}_{-1.3}$	$1.75^{+1.48}_{-0.97}$	2.6	0.0	$45^{+49}_{-13}$
1000	$26.3^{+0.4}_{-1.2}$	$1.16^{+1.29}_{-0.43}$	79	1.9	$122^{+50}_{-71}$

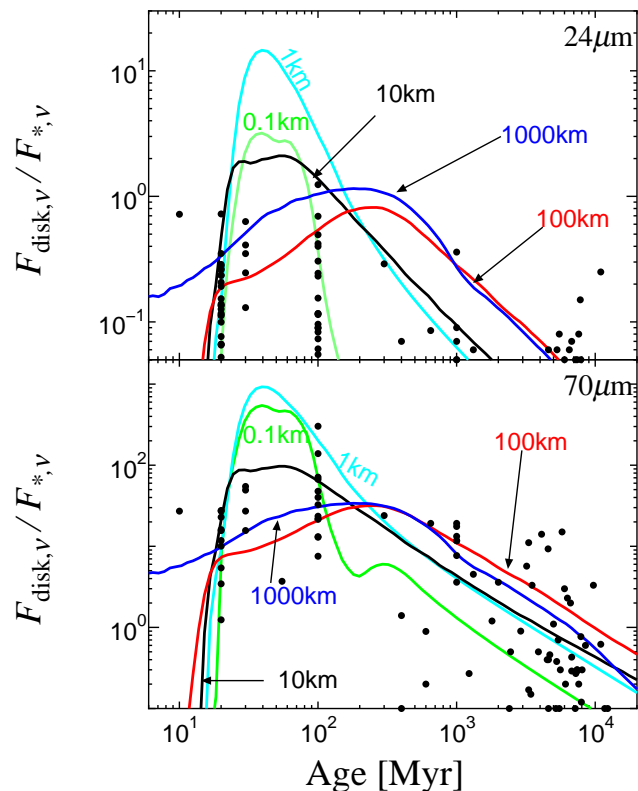


**Figure 11.** Temporal evolution of the flux ratios using best-fit parameter sets listed in Table 1 for initial planetesimal radii of 0.1, 1, 10, 100, 1000 km.

effects of gas even in early times. Even starting with similar initial planetesimals, the time when disc fluxes increase is earlier for our simulation. This means that gas drag plays an important role in flux evolution before 100 million years. Indeed, since collisional cascades cannot effectively produce 1  $\mu\text{m}$ -sized bodies in a gaseous disc (Kobayashi et al. 2010), disc fluxes may not rise before gas depletion occurs.

If gas depletion is taken into account, the inner edge of a disc may also be naturally explained. If discs still have as much gas as the minimum-mass solar nebula, collisional fragmentation between bodies smaller than about 10 m does not occur because of damping due to gas drag. Hence, collisional cascade induced by planet formation do not significantly produce bodies smaller than 10 m and the bodies at the low-mass end of the collisional cascade are depleted by radial drift due to gas drag (Kobayashi et al. 2010; Kobayashi, Tanaka, & Krivov 2011;

Kobayashi, Ormel, & Ida 2012). After gas depletion, collisional cascades can produce smaller bodies and then debris disc fluxes increase. If planet formation occurs inside a radius  $r_{\text{gas}}$  prior to gas depletion, planets are subsequently formed beyond  $r_{\text{gas}}$  in a gas-free disc. If  $r_{\text{gas}}$  corresponds to the inner edge radius  $r_{\text{in}}$  of a planetesimal disc that we assume in this paper, the flux evolution is expected to be similar: The inner edges of planetesimal discs may be related to the gas depletion of protoplanetary discs. On the other hand, gas giant planets formed inside  $r_{\text{in}}$  dynamically clean up around their orbits, which may also contribute to the formation of the inner edges of planetesimal discs.

Planetesimal formation beyond several 10 AU is difficult because radial drift is more rapid than the collisional growth of dust in protoplanetary discs; possible formation region of planetesimals via collisional growth is inside several 10 AU (Okuzumi et al. 2012). On the other hand, if stars are born in a cluster, stars experience close stellar encounters during their escape from the cluster. Such an early stellar encounter truncates the disc; a stellar passage at  $\approx 100$  AU as expected in the relatively dense clusters produces an outer edge of planet forming region at 30 AU (Kobayashi & Ida 2001) and explains some dynamical properties of Kuiper belt objects (Kobayashi, Ida, & Tanaka 2005). Therefore, planetesimal formation and/or an early stellar encounter may explain the outer edges of planetesimal discs.

In the solar system, Jupiter and Saturn were formed before the gas lifetime of the solar nebula, while Uranus and Neptune were formed after significant gas depletion. Planet formation in gas-free discs might have occurred beyond 10–20 AU. An early stellar encounter as an explanation of the orbital distribution of Kuiper belt objects may yield the outer edge of the planetesimal disc at around 50 AU (Kobayashi, Ida, & Tanaka 2005). Therefore, narrow planetesimal discs composed of large planetesimals ( $s_0 \sim 100$  km) that are very likely to form debris discs might be similar to that of the solar system. Taking into account gas depletion, the similarity to the solar system should be addressed in future studies.

We thank A. Mustill for helpful comments that helped to improve our manuscript. HK gratefully acknowledges support from Grants-in-Aid from MEXT (23103005). TL acknowledges support from the Deutsche Forschungsgemeinschaft, grant Lo 1715/1-1.

**REFERENCES**

- Beichman C. A., et al., 2005, *ApJ*, 622, 1160  
 Beichman C. A., et al., 2006, *ApJ*, 652, 1674  
 Benz W., Asphaug E., 1999, *Icar*, 142, 5  
 Bohren C. F., Huffman D. R., 1983, *Absorption and Scattering of Light by Small Particles*, Wiley, New York  
 Bryden G., et al., 2006, *ApJ*, 636, 1098  
 Burns J. A., Lamy P. L., Soter S., 1979, *Icar*, 40, 1  
 Chen C. H., et al., 2005, *ApJ*, 634, 1372  
 Chen C. H., Jura M., Gordon K. D., Blaylock M., 2005, *ApJ*, 623, 493  
 Cuzzi J. N., Hogan R. C., Shariff K., 2008, *ApJ*, 687, 1432  
 Draine B. T., Lee H. M., 1984, *ApJ*, 285, 89  
 Hayashi C., 1981, *PThPS*, 70, 35  
 Hillenbrand L. A., et al., 2008, *ApJ*, 677, 630  
 Ida S., Makino J., 1992, *Icar*, 96, 107  
 Hines D. C., et al., 2006, *ApJ*, 638, 1070  
 Kennedy G. M., Wyatt M. C., 2010, *MNRAS*, 405, 1253  
 Kenyon S. J., Bromley B. C., 2004, *AJ*, 127, 513  
 Kenyon S. J., Bromley B. C., 2008, *ApJS*, 179, 451  
 Kim J. S., et al., 2005, *ApJ*, 632, 659  
 Kimura H., Mann I., Jessberger E. K., 2003, *ApJ*, 583, 314  
 Kobayashi H., Ida S., 2001, *Icar*, 153, 416  
 Kobayashi H., Ida S., Tanaka H., 2005, *Icar*, 177, 246  
 Kobayashi H., Ormel C. W., Ida S., 2012, *ApJ*, 756, 70  
 Kobayashi H., Tanaka H., 2010, *Icar*, 206, 735  
 Kobayashi H., Tanaka H., Krivov A. V., 2011, *ApJ*, 738, 35  
 Kobayashi H., Tanaka H., Krivov A. V., Inaba S., 2010, *Icar*, 209, 836  
 Kobayashi H., Watanabe S.-I., Kimura H., Yamamoto T., 2008, *Icar*, 195, 871  
 Kobayashi H., Watanabe S.-I., Kimura H., Yamamoto T., 2009, *Icar*, 201, 395  
 Li A., Greenberg J. M., 1997, *A&A*, 323, 566  
 Löhne T., Krivov A. V., Rodmann J., 2008, *ApJ*, 673, 1123  
 Meyer M. R., et al., 2004, *ApJS*, 154, 422  
 Moro-Martín A., et al., 2007, *ApJ*, 658, 1312  
 Mustill A. J., Wyatt M. C., 2009, *MNRAS*, 399, 1403  
 Okuzumi S., Tanaka H., Kobayashi H., Wada K., 2012, *ApJ*, 752, 106  
 Ormel C. W., Dullemond C. P., Spaans M., 2010, *Icar*, 210, 507  
 Stewart S. T., Leinhardt Z. M., 2009, *ApJ*, 691, L133  
 Wada K., Tanaka H., Okuzumi S., Kobayashi H., Suyama T., Kimura H., Yamamoto T., 2013, *A&A*, 559, A62  
 Warren S. G., 1984, *ApOpt*, 23, 1206  
 Weidenschilling S. J., 2010, *ApJ*, 722, 1716  
 Wyatt M. C., 2005, *A&A*, 433, 1007